The Astrophysical Journal, 600:670–680, 2004 January 10

Ni ABUNDANCE IN THE CORE OF THE PERSEUS CLUSTER: AN ANSWER TO THE SIGNIFICANCE OF RESONANT SCATTERING

Fabio Gastaldello[1]
IASF-CNR, via Bassini 15, I-20133 Milan, Italy; gasta@mi.iasf.cnr.it

and

Silvano Molendi
IASF-CNR, via Bassini 15, I-20133 Milan, Italy; silvano@mi.iasf.cnr.it
Received 2003 January 27; accepted 2003 September 23

ABSTRACT

Using an *XMM-Newton* observation of the Perseus cluster we show that the excess in the flux of the 7–8 keV line complex previously detected by *ASCA* and *BeppoSAX* is due to an overabundance of nickel rather than to an anomalously high Fe Heβ/Fe Heα ratio. This observational fact leads to the main result that resonant scattering, which was assumed to be responsible for the supposed anomalous Fe Heβ/Fe Heα ratio, is no longer required. The absence of resonant scattering points toward the presence of significant gas motions (either turbulent or laminar) in the core of the Perseus Cluster.

Subject headings: galaxies: abundances — galaxies: clusters: individual (A426, Perseus) — intergalactic medium — scattering — X-rays: galaxies

1. INTRODUCTION

The X-ray emission from clusters is due to a diffuse, tenuous (with typical densities of 10^{-4} to 10^{-2} cm^{-3}), and hot (with typical temperatures of 10^7–10^8 K) thermal plasma. Although for these ranges of density and temperature the gas is optically thin to Thomson scattering for the continuum, it can be optically thick in the resonance X-ray lines of highly ionized atoms of heavy elements (Gilfanov et al. 1987). Apart from other interesting observable effects (Sazonov et al. 2002), the major effect of resonance scattering (the absorption of a line photon followed by immediate reemission) is to distort the surface brightness profile of the cluster in the resonance line due to diffusion of photons from the dense core into the outer regions of the cluster. This must be taken into account when attempting to determine element abundances from X-ray spectroscopic observations of galaxy clusters. In fact, only with the key assumption that the plasma is optically thin can line equivalent widths unambiguously convert to element abundances when fitting CCD spectra with the available plasma codes. In the presence of resonant scattering the true abundances in the core of clusters are significantly underestimated since the line emission is attenuated because photons are scattered out of the line of sight. To make things worse, the most promising line for resonant scattering is the Heα Fe emission line at 6.7 keV (Gilfanov et al. 1987; Sazonov et al. 2002), which is also one of the most prominent emission lines in the cluster spectra and in general drives the global abundance determination.

High-sensitivity and high-resolution spectrometers are needed to directly measure the spectral features of resonant scattering (as a modification of the line profile or resolution of the He-like line into its constituents in order to determine directly the effects of scattering) and polarimeters, to detect the polarized scattered radiation (Costa et al. 2001; Sazonov et al. 2002). Currently the simplest method for revealing and estimating the presence of resonance scattering is to compare the fluxes of an expected optically thick line and of an optically thin one and to check whether it is correctly modeled by a plasma code assuming optically thin emission. This was done in the past with *ASCA* and *BeppoSAX* for the ratio between Heα Fe line at 6.7 keV and the Heβ Fe line at 7.90 keV (which is expected to have an optical depth typically smaller than one for resonant scattering), and in particular the best data were the ones for the Perseus Cluster.

Molendi et al. (1998) analyzed data collected with the MECS on board *BeppoSAX* and found that the ratio of the flux of the 7–8 keV line complex to the 6.7 keV line was significantly larger than predicted by the optically thin plasma code and that the ratio decreases with increasing cluster radius. They noted that this effect could be explained either by resonant scattering or by a Ni overabundance, eventually favoring the former explanation. On the contrary, Dupke & Arnaud (2001), according to the experimental evidence of a central enhancement of SN Ia ejecta in cD clusters, favored the overabundant Ni explanation.

These were the two hypotheses that the resolution and sensitivity of past instruments could not resolve. *XMM-Newton* has now for the first time provided a combination of resolution and effective area at high energies to give an unambiguous answer to the question. In this paper our aim is to try to solve this controversy. A complete spectral and spatial analysis, in particular of the temperature structure of the Perseus Cluster, which requires a detailed temperature map, is beyond the scope of this paper.

The outline of the paper is as follows. In § 2 we give information about the *XMM-Newton* observation and data preparation. In § 3 we present spatially resolved measurements of temperature and Ni and Fe abundances. In § 4 we discuss our results and draw our conclusions.

At the nominal redshift of Perseus ($z = 0.0183$), $1'$ corresponds to 22.2 kpc ($H_0 = 70$ km s^{-1} Mpc^{-1} and $\Omega_m = 1 - \Omega_\Lambda = 0.3$). In the following analysis, all the quoted errors are at 1 σ (68.3% confidence level) unless stated otherwise.

[1] Università di Milano Bicocca, Dipartimento di Fisica, Piazza della Scienza 3 I-20133 Milan, Italy.

2. OBSERVATION AND DATA PREPARATION

The Perseus Cluster was observed with *XMM-Newton* (Jansen et al. 2001) during revolution 210, with the THIN1 filter and in full-frame mode, for 53.6 ks for MOS and 51.2 ks for the PN camera, but resulting in an effective exposure time (as written in the keyword LIVETIME of the fits event file) of 53.1 ks for the MOS and 24.7 ks for the PN camera. We generated calibrated event files using the publicly available SASv5.3.3.

To fully exploit the excellent EPIC data from extended and low surface brightness objects and from this observation in particular, the EPIC background needs to be correctly taken into account. The EPIC background can be divided into a cosmic X-ray background, dominant below 2–3 keV, and an instrumental background, dominant for energies higher than 2–3 keV (for the continuum emission, apart from fluorescence lines). This latter component can be further divided into a detector noise component, present in the low-energy range (below 300 eV) and in a particle-induced background, which is the major concern for our scientific case. The particle-induced background consists of a flaring component, characterized by strong and rapid variability, produced by soft protons (with energies of less than few hundreds of keV), which are funneled toward the detectors by the mirrors, and a second more stable component associated with high-energy particles interacting with the structure surrounding the detectors and the detectors themselves. The latter component has been studied using CLOSED filter observation, shows only small intensity variations, and is characterized by a flat spectrum and a number of fluorescent lines. Apart from a rather strong variability of the fluorescent lines, this component can be properly subtracted using a large collection of background data. The common way to face the flaring component is to remove periods of high background, because the signal-to-noise ratio (S/N) is highly degraded, especially at high energy (where the data are crucial to measure the exponential cutoff and thus the temperature of the emitting plasma) and because the shape of the spectrum is varying with time (Arnaud et al. 2001). The strategies for rejecting these flaring periods are mainly two: selection of time intervals where the count rate in a given high-energy band is lower than a given threshold (which has been our approach in a previous analysis where we fixed the thresholds at 0.35 counts s^{-1} for the PN camera in the 10–13 keV band and 0.15 counts s^{-1} in the 10–12 keV band for MOS, based on Lockman Hole data) or finding a mean count $\overline{c}$ and then choosing as a threshold value $\overline{c} + 3\ \sigma$, by means of a Gaussian or Poissonian fitting or σ clipping methods (see Appendix A of Pratt & Arnaud [2002] for the second approach and Marty et al. [2002] for a general discussion on soft proton cleaning criteria).

The light curve in the 10–13 keV band for the PN observation of the Perseus Cluster is shown in Figure 1 together with our standard threshold of 0.35 counts s^{-1}. It is evident that the observation is badly affected by soft protons, and if we adopt our threshold all the observation would be rejected. The light curve is also structured in such a way that a 3 σ clipping method rejects only 529 s of observation, finding a mean rate of 0.53 counts s^{-1} with a standard deviation of 0.15 counts s^{-1}, while fitting with a Gaussian and rejecting all the intervals above 3 σ from the mean rejects only 700 s of observation. Our approach was therefore to consider the effective area file for two reasons: (1) we can exploit the fact that Perseus is the brightest X-ray cluster and is so bright in its central zone that the background, also in the presence of a high level of soft protons such as we have in our observation, is not important; moreover, (2) we can try to model the soft protons that contaminate the spectra by using in first approximation a power law as a background model (which means that the model is not convolved via the effective area of the instrument). The self-consistency and viability of our approach will be shown in the results.

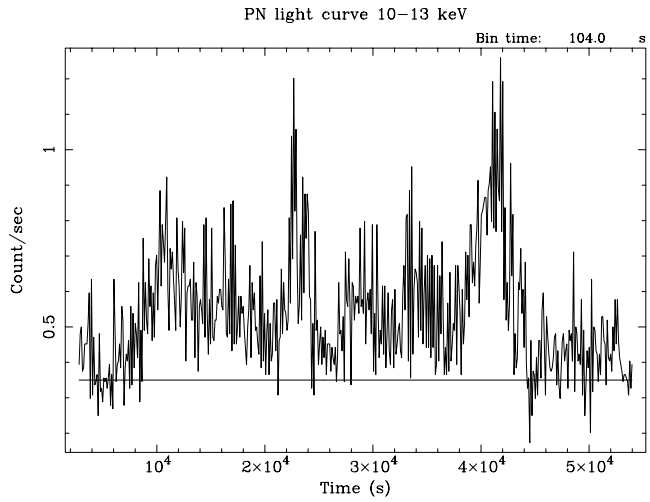

FIG. 1.—PN light curve in the energy band 10–13 keV, together with our threshold of 0.35 counts s^{-1}.

We have accumulated spectra in nine concentric annular regions centered on the emission peak with bounding radii of 0.′5–1′, 1′–2′, 2′–3′, 3′–4′, 4′–5′, 5′–6′, 6′–8′, 8′–10′, and 10′–14′. We did not consider the inner bin inside 0.′5, in order to avoid contamination by the power-law spectrum of the Seyfert cD galaxy NGC 1275. Spectra have been accumulated for the three cameras independently, and the blank fields provided by the calibration teams were used as background. Background spectra have been accumulated from the same sky regions as the source spectra, after reprojection onto the sky attitude of the source (this ensures proper subtraction in the same way as it was performed in detector coordinates).[2]

The vignetting correction has been applied to the effective area generating effective area files for the different annular regions using the SAS task *arfgen*. We generate a flux-weighted area file using exposure-corrected images of the source as detector maps and the parameter extended source switched to true, following the prescription of Saxton & Siddiqui.[3] Spectral results for the cluster A3528 obtained in this way and with the vignetting correction applied directly to the spectra (Arnaud et al. 2001) are practically the same (Gastaldello et al. 2003). We also correct the PN spectra for out-of-time events following the prescriptions of Grupe.[4] The redistribution matrices used are m1_r6_all_15.rmf (MOS1), m2_r6_all_15.rmf (MOS2) and, depending on the mean "RAWY" of the region, the set of 10 single-pixel matrices, from epn_ff20_sY0.rmf to epn_ff20_sY9.rmf, and double-pixel matrices, from epn_ff 20_ dY0.rmf to epn_ff 20_dY9.rmf, for PN.

[2] See D. Lumb 2002, EPIC background files at http://xmm.vilspa.esa.es/docs/documents/CAL-TN-0016-1-0.ps.gs.

[3] See R. D. Saxton & H. Siddiqui 2002 at http://xmm.vilspa.esa.es/docs/documents/PS-TN-0043-3-0.ps.gz

[4] See D. Grupe 2001 at http://wave.xray.mpe.mpg.de/xmm/cookbook/EPICPN/ootevents.html.

Because of its higher effective area (further increased by the use of doubles data) and similar spectral resolution at high energies, the PN camera will be the leading instrument in our analysis and the one for which the results are most compelling, in particular for what concerns the Ni abundance. There are still some problems for what concerns the three EPIC cameras' cross-calibration, and, in particular, at high energies the study of power-law sources returns harder spectra for MOS1, intermediate spectra for MOS2, and then the softest spectra for PN.[5] Also, our analysis of the galaxy cluster A3528 gives systematically higher temperatures and abundances for MOS1 than for MOS2 and PN. The conclusions of a recent work aimed at assessing the EPIC spectral calibration using a simultaneous *XMM-Newton* and *BeppoSAX* observation of 3C 273 strengthen this fact: the MOS-PN cross-calibration has been achieved to the available statistical level except for the MOS1 in the 3–10 keV band, which returns a flatter spectral slope.[6]

3. SPECTRAL MODELING AND ENERGY RANGES USED

All spectral fitting has been performed using version 11.2.0 of the XSPEC package (Arnaud 1996).

As a first step we concentrate on the hard band, which is the one of interest for determining the abundances of iron and nickel and also for making a direct comparison with the MECS results. We use three different energy bands: 3–10, 3–7 keV in order to have a band less contaminated by the hard tail of soft protons, and the 3–13.5 and 3–12 keV for PN and MOS, respectively, in order to have more data to acceptably model the soft protons background.

When fitting the first two bands, we analyze the spectra with a one-temperature (1T) VMEKAL model (Mewe et al. 1985; Kaastra 1992; Liedahl, Osterheld, & Goldstein 1995) with the multiplicative component WABS to account for the Galactic absorption fixed at the value of 0.143×10^{22} cm^{-2} (according to Schmidt et al. 2002). We leave the abundances of Ar, Ca, Fe, and Ni (the only elements that have emission lines in the range 3–10 keV) free and keep all the other abundances fixed to half the solar values [Fukazawa et al. 2000; this corresponds for example to the 1T (3–10 keV) model in Tables 1 and 2].

When fitting the wider high-energy band, more contaminated by soft protons, we add a power-law background model (VMEKAL+POW/B in XSPEC) in order to model the soft-proton background component [this corresponds to the 1T+pow (3–13.5 keV) model in Table 1 and 1T+pow/b (3–12 keV) in Table 2].

As a second step we fit the entire energy band 0.5–10 keV with two models:

1. A 1T model that leaves $N_{\rm H}$ to vary freely (the fit is substantially improved with respect to the one with $N_{\rm H}$ fixed to the Galactic value) and the abundance of O, Ne, Mg, Si, S, Ar, Ca, Fe, and Ni. For the outer annuli, when required from the previous analysis in the hard band, we add the pow/b component with normalization and slope fixed at the best-fit

[5] See M. Kirsch et al. 2002, status of the EPIC calibration and data analysis, at http://xmm.vilspa.esa.es/docs/documents/CAL-TN-0018-2-1.pdf.

[6] See S. Molendi & S. Sembay 2003, at http://xmm.vilspa.esa.es/docs/documents/CAL-TN-0036-1-0.ps.gz.

TABLE 1

PARAMETERS VALUES FOR 1T AND 2T MODELS IN DIFFERENT ENERGY BANDS FOR THE INNER RINGS OF THE PERSEUS CLUSTER USING THE SINGLE EVENTS OF THE PN CAMERA

Bin	Model/Band (keV)	$N_{\rm H}$	kT_h	EM$_h$	kT_c	EM$_c$	Fe	Ni	χ^2/dof
0′.5–1′	1T+pow/b (3–13.5)	...	$3.91^{+0.11}_{-0.04}$	$4.99^{+0.03}_{-0.09}$	...	...	$0.62^{+0.01}_{-0.01}$	$1.53^{+0.27}_{-0.24}$	845/809
	1T (3–10)	...	$3.99^{+0.05}_{-0.06}$	$4.91^{+0.02}_{-0.03}$	...	...	$0.62^{+0.01}_{-0.01}$	$1.48^{+0.27}_{-0.24}$	834/799
	1T (0.5–10)	$1.09^{+0.01}_{-0.01}$	$3.29^{+0.01}_{-0.01}$	$5.75^{+0.01}_{-0.01}$	...	...	$0.80^{+0.01}_{-0.01}$	$1.38^{+0.11}_{-0.15}$	2037/1299
	2T (0.5–10)	$1.15^{+0.01}_{-0.01}$	$5.00^{+0.08}_{-0.01}$	$3.07^{+0.02}_{-0.03}$	$2.03^{+0.02}_{-0.01}$	$2.90^{+0.04}_{-0.07}$	$0.69^{+0.01}_{-0.01}$	$1.06^{+0.11}_{-0.10}$	1734/1297
1′–2′	1T+pow/b (3–13.5)	...	$4.01^{+0.04}_{-0.04}$	$11.3^{+0.1}_{-0.1}$	...	...	$0.65^{+0.01}_{-0.01}$	$1.23^{+0.16}_{-0.16}$	1114/1051
	1T (3–10)		$4.13^{+0.06}_{-0.02}$	$11.2^{+0.1}_{-0.1}$	...	...	$0.64^{+0.01}_{-0.01}$	$1.24^{+0.15}_{-0.17}$	1091/1020
	1T (0.5–10)	$1.12^{+0.01}_{-0.01}$	$3.58^{+0.01}_{-0.01}$	$12.19^{+0.01}_{-0.02}$	...	...	$0.80^{+0.01}_{-0.01}$	$1.42^{+0.10}_{-0.09}$	2894/1520
	2T (0.5–10)	$1.17^{+0.01}_{-0.01}$	$4.95^{+0.02}_{-0.03}$	$7.97^{+0.03}_{-0.05}$	$2.04^{+0.01}_{-0.02}$	$4.77^{+0.08}_{-0.03}$	$0.71^{+0.01}_{-0.01}$	$1.16^{+0.06}_{-0.10}$	2371/1518
2′–3′	1T+pow/b (3–13.5)	...	$4.86^{+0.07}_{-0.04}$	$8.89^{+0.10}_{-0.13}$	...	...	$0.61^{+0.01}_{-0.01}$	$0.85^{+0.15}_{-0.17}$	1079/1063
	1T (3–10)	...	$4.99^{+0.06}_{-0.04}$	$8.83^{+0.07}_{-0.03}$	...	...	$0.61^{+0.01}_{-0.01}$	$0.91^{+0.16}_{-0.17}$	1039/1020
	1T (0.5–10)	$1.14^{+0.01}_{-0.01}$	$4.28^{+0.01}_{-0.02}$	$9.74^{+0.01}_{-0.04}$			$0.72^{+0.01}_{-0.01}$	$1.24^{+0.13}_{-0.12}$	2349/1519
	2T (0.5–10)	$1.18^{+0.01}_{-0.01}$	$5.95^{+0.04}_{-0.03}$	$7.22^{+0.03}_{-0.06}$	$2.11^{+0.02}_{-0.01}$	$2.86^{+0.08}_{-0.02}$	$0.67^{+0.01}_{-0.01}$	$1.08^{+0.09}_{-0.12}$	1978/1517
3′–4′	1T+pow/b (3–13.5)	...	$5.52^{+0.08}_{-0.07}$	$6.44^{+0.04}_{-0.04}$	...	...	$0.56^{+0.01}_{-0.01}$	$0.80^{+0.19}_{-0.19}$	1061/1080
	1T (3–10)	...	$6.03^{+0.08}_{-0.09}$	$6.36^{+0.03}_{-0.03}$	...	...	$0.56^{+0.01}_{-0.01}$	$0.87^{+0.16}_{-0.17}$	1062/1027
	1T+pow/b (0.5–10)	$1.15^{+0.01}_{-0.01}$	$4.99^{+0.02}_{-0.03}$	$6.93^{+0.01}_{-0.02}$	...	...	$0.61^{+0.01}_{-0.01}$	$1.09^{+0.15}_{-0.15}$	2040/1527
	2T+pow/b (0.5–10)	$1.19^{+0.01}_{-0.01}$	$5.64^{+0.02}_{-0.04}$	$6.25^{+0.03}_{-0.02}$	$1.64^{+0.03}_{-0.01}$	$0.79^{+0.01}_{-0.04}$	$0.56^{+0.03}_{-0.01}$	$1.06^{+0.15}_{-0.12}$	1914/1525
4′–5′	1T+pow/b (3–13.5)	...	$5.97^{+0.08}_{-0.09}$	$5.67^{+0.08}_{-0.06}$	...	...	$0.52^{+0.01}_{-0.01}$	$0.71^{+0.21}_{-0.20}$	1210/1090
	1T+pow/b (0.5–10)	$1.13^{+0.02}_{-0.01}$	$5.57^{+0.02}_{-0.03}$	$5.99^{+0.01}_{-0.02}$			$0.55^{+0.01}_{-0.01}$	$0.81^{+0.18}_{-0.16}$	1960/1521
	2T+pow/b (0.5–10)	$1.19^{+0.01}_{-0.01}$	$6.26^{+0.04}_{-0.03}$	$5.49^{+0.03}_{-0.01}$	$1.61^{+0.03}_{-0.04}$	$0.60^{+0.01}_{-0.03}$	$0.53^{+0.03}_{-0.01}$	$0.78^{+0.11}_{-0.12}$	1877/1519
5′–6′	1T+pow/b (3–13.5)	...	$6.36^{+0.14}_{-0.11}$	$4.69^{+0.02}_{-0.03}$	...	...	$0.49^{+0.01}_{-0.01}$	$0.50^{+0.25}_{-0.24}$	1095/1072
	1T+pow/b (0.5–10)	$1.13^{+0.01}_{-0.01}$	$5.65^{+0.02}_{-0.05}$	$5.06^{+0.01}_{-0.02}$	...	...	$0.50^{+0.01}_{-0.01}$	$1.14^{+0.21}_{-0.18}$	2004/1497
	2T+pow/b (0.5–10)	$1.18^{+0.01}_{-0.01}$	$6.36^{+0.06}_{-0.06}$	$4.69^{+0.02}_{-0.01}$	$1.37^{+0.03}_{-0.01}$	$0.42^{+0.01}_{-0.03}$	$0.47^{+0.02}_{-0.01}$	$1.24^{+0.14}_{-0.23}$	1898/1495
6′–8′	1T+pow/b (3–13.5)	...	$6.78^{+0.13}_{-0.11}$	$7.44^{+0.11}_{-0.20}$	...	...	$0.47^{+0.01}_{-0.01}$	$0.12^{+0.23}_{-0.11}$	1249/1289
	1T+pow/b (0.5–10)	$1.15^{+0.01}_{-0.01}$	$5.85^{+0.03}_{-0.04}$	$8.04^{+0.01}_{-0.02}$			$0.49^{+0.03}_{-0.01}$	$0.93^{+0.20}_{-0.17}$	2274/1637
	2T+pow/b (0.5–10)	$1.21^{+0.01}_{-0.01}$	$6.69^{+0.04}_{-0.06}$	$7.50^{+0.02}_{-0.02}$	$1.29^{+0.01}_{-0.03}$	$0.63^{+0.02}_{-0.02}$	$0.47^{+0.01}_{-0.01}$	$1.27^{+0.12}_{-0.23}$	2009/1635

NOTE.—All errors quoted are at the 68% level for one interesting parameter ($\Delta\chi^2 = 1$).

TABLE 2

PARAMETERS VALUES FOR 1T AND 2T MODELS IN DIFFERENT ENERGY BANDS FOR THE INNER RINGS OF THE PERSEUS CLUSTER USING THE THE MOS2 CAMERA

Bin	Model/Band (keV)	$N_{\rm H}$	kT_h	EM$_h$	kT_c	EM$_c$	Fe	Ni	χ^2/dof
0.′5–1′	1T+pow/b (3–12)	...	$3.84^{+0.06}_{-0.04}$	$5.36^{+0.02}_{-0.03}$	...	...	$0.64^{+0.03}_{-0.01}$	$0.76^{+0.34}_{-0.29}$	385/323
	1T (3–10)	...	$3.86^{+0.07}_{-0.03}$	$5.37^{+0.02}_{-0.03}$	...	...	$0.64^{+0.03}_{-0.01}$	$0.83^{+0.30}_{-0.30}$	372/318
	1T (0.5–10)	$1.17^{+0.01}_{-0.01}$	$3.38^{+0.01}_{-0.02}$	$5.91^{+0.01}_{-0.01}$	...	...	$0.81^{+0.01}_{-0.01}$	$1.04^{+0.18}_{-0.09}$	810/479
	2T (0.5–10)	$1.20^{+0.02}_{-0.01}$	$5.18^{+0.05}_{-0.06}$	$2.82^{+0.03}_{-0.09}$	$2.33^{+0.02}_{-0.02}$	$3.26^{+0.25}_{-0.08}$	$0.74^{+0.01}_{-0.01}$	$0.88^{+0.12}_{-0.10}$	669/477
1′–2′	1T+pow/b (3–12)	...	$4.14^{+0.05}_{-0.06}$	$12.2^{+0.1}_{-0.1}$	...	...	$0.72^{+0.01}_{-0.01}$	$0.77^{+0.20}_{-0.21}$	436/393
	1T (3–10)	...	$4.20^{+0.05}_{-0.05}$	$12.1^{+0.1}_{-0.2}$	...	...	$0.71^{+0.01}_{-0.01}$	$0.80^{+0.21}_{-0.20}$	435/379
	1T (0.5–10)	$1.18^{+0.01}_{-0.01}$	$3.67^{+0.01}_{-0.01}$	$13.00^{+0.01}_{-0.02}$	...	...	$0.86^{+0.01}_{-0.01}$	$1.09^{+0.11}_{-0.09}$	1228/540
	2T (0.5–10)	$1.19^{+0.01}_{-0.01}$	$6.68^{+0.06}_{-0.09}$	$4.09^{+0.03}_{-0.14}$	$2.91^{+0.01}_{-0.01}$	$9.15^{+0.06}_{-0.05}$	$0.83^{+0.01}_{-0.01}$	$0.98^{+0.11}_{-0.09}$	966/538
2′–3′	1T+pow/b (3–12)	...	$4.96^{+0.06}_{-0.11}$	$10.00^{+0.15}_{-0.05}$	...	...	$0.64^{+0.01}_{-0.01}$	$0.49^{+0.22}_{-0.21}$	406/402
	1T (3–10)	...	$5.17^{+0.05}_{-0.09}$	$9.83^{+0.12}_{-0.07}$	...	...	$0.65^{+0.01}_{-0.02}$	$0.59^{+0.24}_{-0.20}$	415/383
	1T (0.5–10)	$1.17^{+0.01}_{-0.01}$	$4.35^{+0.02}_{-0.01}$	$10.96^{+0.02}_{-0.01}$	...	...	$0.72^{+0.01}_{-0.01}$	$1.16^{+0.15}_{-0.11}$	1106/544
	2T (0.5–10)	$1.21^{+0.01}_{-0.01}$	$5.78^{+0.05}_{-0.03}$	$7.84^{+0.05}_{-0.07}$	$2.32^{+0.03}_{-0.02}$	$3.43^{+0.08}_{-0.06}$	$0.69^{+0.01}_{-0.01}$	$0.92^{+0.12}_{-0.10}$	841/542
3′–4′	1T+pow/b (3–12)	...	$5.78^{+0.09}_{-0.10}$	$7.54^{+0.09}_{-0.07}$	...	...	$0.61^{+0.01}_{-0.01}$	$0.81^{+0.26}_{-0.25}$	407/406
	1T (3–10)	...	$6.15^{+0.09}_{-0.11}$	$7.37^{+0.06}_{-0.05}$	...	...	$0.62^{+0.01}_{-0.02}$	$1.03^{+0.26}_{-0.25}$	415/380
	1T+pow/b (0.5–10)	$1.17^{+0.02}_{-0.01}$	$5.25^{+0.04}_{-0.02}$	$7.93^{+0.01}_{-0.01}$	...	...	$0.67^{+0.01}_{-0.01}$	$1.17^{+0.22}_{-0.15}$	782/542
	2T+pow/b (0.5–10)	$1.21^{+0.01}_{-0.01}$	$6.30^{+0.05}_{-0.10}$	$5.31^{+0.03}_{-0.08}$	$2.74^{+0.05}_{-0.11}$	$1.47^{+0.14}_{-0.06}$	$0.64^{+0.01}_{-0.02}$	$0.98^{+0.18}_{-0.15}$	687/540
4′–5′	1T+pow/b (3–12)	...	$6.14^{+0.12}_{-0.17}$	$6.09^{+0.06}_{-0.07}$	...	...	$0.55^{+0.01}_{-0.01}$	$0.38^{+0.33}_{-0.30}$	412/401
	1T+pow/b (0.5–10)	$1.26^{+0.01}_{-0.02}$	$5.60^{+0.03}_{-0.04}$	$6.37^{+0.01}_{-0.02}$	...	...	$0.58^{+0.01}_{-0.01}$	$1.29^{+0.21}_{-0.23}$	701/538
	2T+pow/b (0.5–10)	$1.27^{+0.02}_{-0.01}$	$6.66^{+0.04}_{-0.11}$	$6.62^{+0.05}_{-0.07}$	$2.36^{+0.06}_{-0.07}$	$1.13^{+0.12}_{-0.04}$	$0.58^{+0.01}_{-0.02}$	$1.23^{+0.19}_{-0.24}$	666/536
5′–6′	1T+pow/b (3–12)	...	$6.67^{+0.23}_{-0.20}$	$4.83^{+0.06}_{-0.05}$	...	...	$0.58^{+0.03}_{-0.03}$	$1.00^{+0.40}_{-0.42}$	363/382
	1T+pow/b (0.5–10)	$1.16^{+0.01}_{-0.01}$	$6.17^{+0.05}_{-0.07}$	$5.01^{+0.02}_{-0.01}$	...	...	$0.59^{+0.01}_{-0.03}$	$1.58^{+0.28}_{-0.33}$	650/518
	2T+pow/b (0.5–10)	$1.18^{+0.02}_{-0.02}$	$7.11^{+0.07}_{-0.19}$	$4.22^{+0.05}_{-0.06}$	$3.31^{+0.15}_{-0.18}$	$0.89^{+0.12}_{-0.09}$	$0.59^{+0.01}_{-0.03}$	$1.36^{+0.32}_{-0.27}$	639/516
6′–8′	1T+pow/b (3–12)	...	$7.20^{+0.21}_{-0.21}$	$7.88^{+0.09}_{-0.09}$	...	...	$0.52^{+0.03}_{-0.03}$	$0.46^{+0.40}_{-0.39}$	447/475
	1T+pow/b (0.5–10)	$1.20^{+0.02}_{-0.01}$	$6.50^{+0.06}_{-0.04}$	$8.27^{+0.01}_{-0.02}$	...	...	$0.53^{+0.01}_{-0.01}$	$1.17^{+0.28}_{-0.26}$	848/572
	2T+pow/b (0.5–10	$1.23^{+0.02}_{-0.02}$	$7.98^{+0.09}_{-0.14}$	$6.95^{+0.06}_{-0.18}$	$2.74^{+0.07}_{-0.14}$	$1.46^{+0.23}_{-0.03}$	$0.55^{+0.01}_{-0.01}$	$1.07^{+0.25}_{-0.26}$	798/570

NOTE.—All errors quoted are at the 68% level for one interesting parameter ($\Delta\chi^2 = 1$).

values found [these models corresponds to 1T (0.5–10 keV) or 1T+pow (0.5–10 keV) in Tables 1 and 2].

2. A 2T model [WABS*(VMEKAL+VMEKAL) in XSPEC], where the metal abundance of each element of the second thermal component is bound to be equal to the same parameter of the first thermal component. As for the 1T model, we add the pow component when required [these models corresponds to 2T (0.5–10 keV) or 2T+pow (0.5–10 keV) in Tables 1 and 2].

The 2T model is a rough attempt to reproduce the complex spectrum resulting from projection effects, the azimuthal mean of very different emission regions (like holes and luminous regions in the Perseus Cluster [see Schmidt et al. 2002; Fabian et al. 2002]), and an atmosphere probably containing components at different temperatures, as in M87 (Kaiser 2003; Molendi 2002).

We also allow the redshift to be a free parameter in order to account for any residual gain calibration problem. We adopt for the solar abundances the values of Grevesse & Sauval (1998), where Fe/H is 3.16×10^{-5}. To compare with previous measurements, a simple rescaling can be made to obtain the values with the set of abundances of Anders & Grevesse (1989), where the solar Fe abundance relative to H is 4.68×10^{-5} by number.

4. RESULTS

4.1. *1T Results in the High-Energy Band*

In Figure 2 we show the temperature profile obtained analyzing the single-event spectrum for the PN camera. This is also an example of our working procedure. The filled circles refer to the results obtained using the 3–10 keV band, while

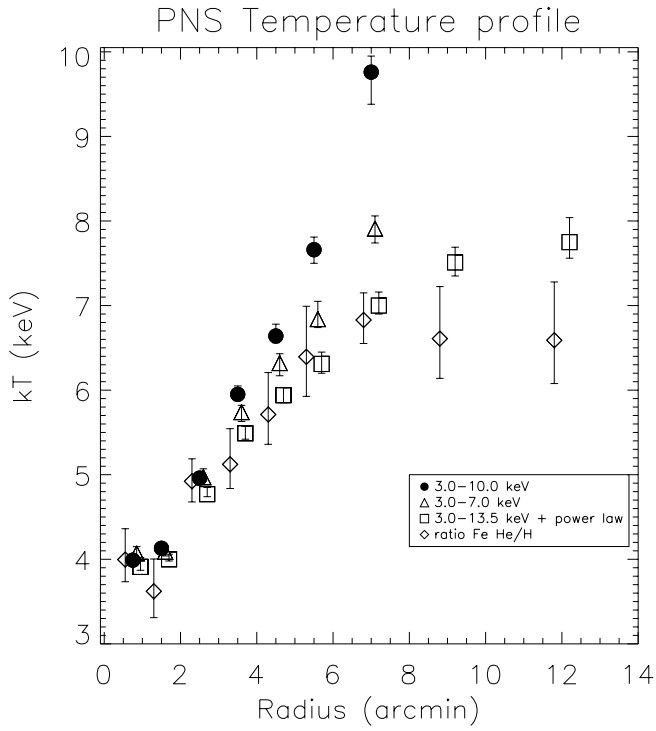

FIG. 2.—PN 1T profile. Uncertainties are at the 68% level for one interesting parameter ($\Delta\chi^2 = 1$). Filled circles represent the temperature obtained using the range 3–10 keV, open triangles represent the temperature obtained using the range 3–7 keV, and open squares represent the temperature obtained by using the range 3–13.5 keV and adding to the source model a power-law background component. In the last two bins we do not show the temperatures obtained in the 3–10 keV and 3–7 keV bands because they are larger than 10 keV. Diamonds represent the temperature obtained by the ratio of the fluxes of Heα to Hα Fe lines.

the open triangles indicates the results obtained using the 3–7 keV band with the Ni abundance frozen to the best-fit value obtained in the 3–10 keV band. It is clear that where the source is overwhelmingly bright, the hard component of the soft proton does not affect the spectrum, and there are no differences between the temperatures obtained in different energy bands while in the outskirts of the cluster; where the source brightness is lower and the soft protons become important, the fitted plasma temperature reaches uncorrect and unphysically high values, and large residuals at high energy are present. With the open squares we show the temperature obtained by fitting not only the source but also the soft protons with a power-law background model in the energy band 3–13.5 keV: as we expect, in the inner region adding the background component does not affect the temperature determination or statistically improve the fit; on the contrary, in the outer regions, the temperature is significantly reduced and the fit is improved, eliminating the residuals at high energies. For example in the $6'$–$8'$ ring the simple 1T fit gives a χ^2 of 1502 for 1137 degrees of freedom (dof), while the fit with the power-law background model in addition gives a χ^2 of 1258 for 1288 dof.

To confirm our results we compare the temperatures obtained in this way with those obtained with the MECS instrument on board *BeppoSAX* (De Grandi & Molendi 2002a). The temperature profiles, shown in Figure 3, apart from the differences in the three cameras due to the cross-calibration problems discussed above (confirmed also with the superb statistics of Perseus), are in good agreement at least up to $8'$. In the outer rings, between $8'$ and $14'$, the increasing importance of background relative to source counts prevents us from recovering a correct temperature with our method (see De Grandi & Molendi 2002a for a more general discussion of *XMM-Newton* and *BeppoSAX* temperature determinations and the greater sensitivity of the latter over the former to low surface brightness regions due to much lower background).

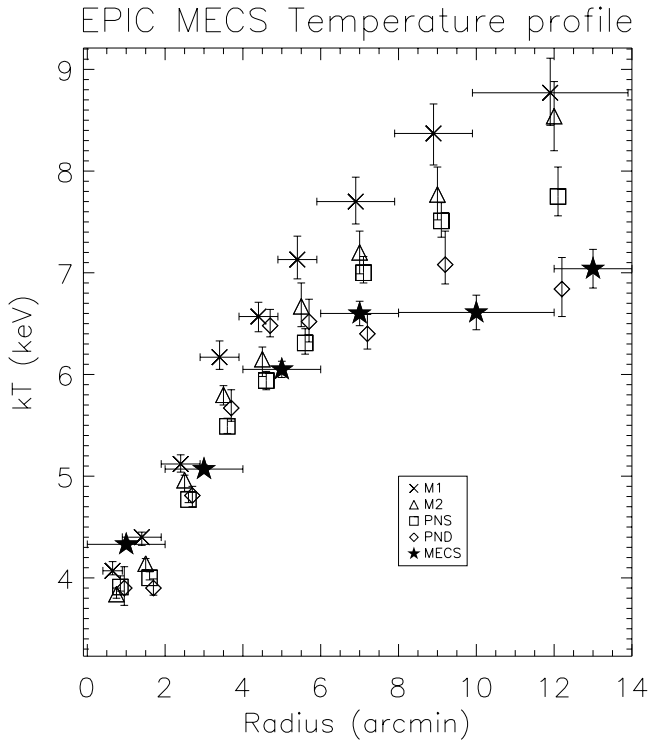

FIG. 3.—Temperature profiles obtained with the various EPIC cameras compared with the temperature profile obtained with the MECS instrument on board *BeppoSAX*. Uncertainties are at the 68% level for one interesting parameter ($\Delta\chi^2 = 1$). Crosses, open triangles, open squares, open diamonds, and filled stars represent temperatures obtained with MOS1, MOS2, PN singles, PN doubles, and the MECS, respectively.

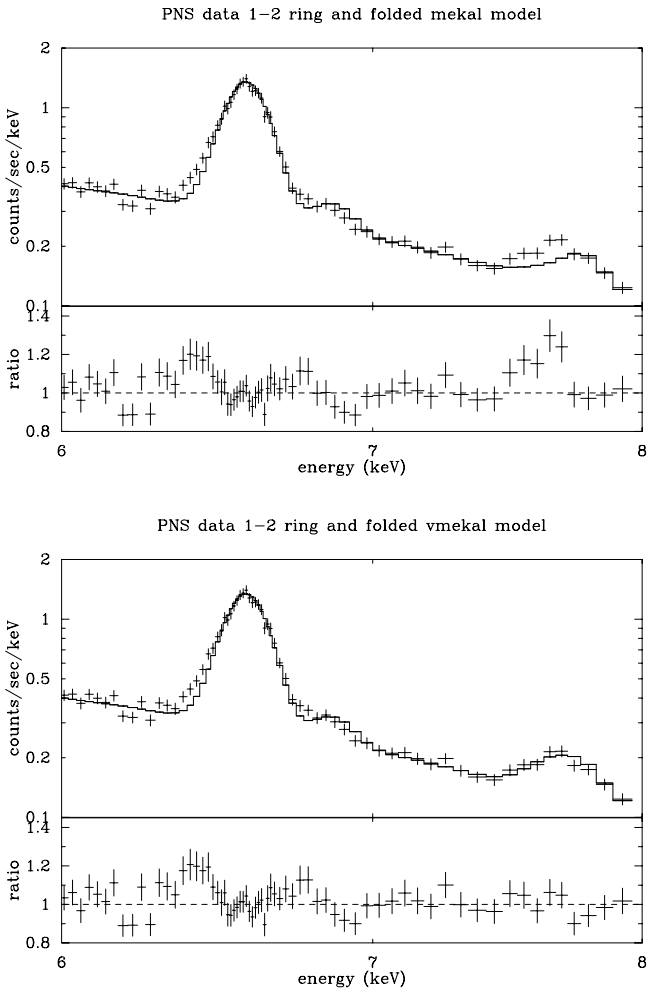

FIG. 4.—PN singles data for the $1'$–$2'$ bin in the 6–8 keV band and the corresponding fit with a MEKAL model, on the top, and with a VMEKAL model, on the bottom, together with the corresponding ratios of data respect to models.

With a determination of the temperature structure we can address the issue of the metal abundance measure and attempt to discriminate between the presence of resonant scattering or the supersolar abundance of nickel. Resonant scattering is increasingly important toward the center of the cluster, so we choose our two inner bins to test its presence. Fitting the spectra with a MEKAL model, assuming solar ratios, actually does not reproduce the 8 keV line complex. As shown in the left panel of Figure 4, for the $1'$–$2'$ bin, the emission is underestimated as for previous missions (see Fig. 1 of Molendi et al. 1998 for an example). However, the data show for the first time that the excess is due to an uncorrect modeling of the Ni Heα line complex at 7.75–7.80 keV (in the rest frame of the source) and not to an underestimation of the Fe Heβ line, which is correctly modeled. In fact, if we fit the data with a VMEKAL model, we eliminate almost completely the residuals and give a better fit with a Ni abundance of 1.23 in solar units, as shown in the right panel of Figure 4. The fit with a MEKAL model gives a χ^2 of 855 for 802 dof for the

0.′5–1′ bin and 1116 for 1023 dof for the 1′–2′ bin, while a fit with a VMEKAL model (with Ar and Ca fixed to 0.5 $Z/Z_{\odot}$, because they are not important in driving the fit, in order to have only the Ni abundance as additional free parameter) gives a χ^2 of 835 for 801 dof for the first bin and 1092 for 1022 dof for the second bin, with values of $\Delta\chi^2$ that are statistically significant at more that the 99.9% according to the F-test (the value of the F statistics is $F = 19.2$, with a probability of exceeding F of 1.4×10^{-5}, for the first bin, and $F = 22.5$, with a probability of exceeding F of 2×10^{-6}, for the second bin).

We can conclude that the ratio of Heβ/Heα Fe lines is not anomalously high with respect to the optically thin model and that it is not necessary to invoke resonant scattering in the core of the Perseus Cluster. The excess in the flux in the 8 keV line complex respect to a MEKAL model is entirely due to Ni overabundance with respect to solar values, as was previously suggested (Dupke & Arnaud 2001).

The reader will notice some residuals in the Heα Fe line complex at 6.7 keV. This is an instrumental artifact present only in the inner bins out to 2′ of the PN camera, which we suspect is connected to some residual CTI problems due to the high flux of the Perseus Cluster. The net effect is to lower the energy resolution broadening the line profile. We test that this does not affect our results by fitting spectra for our two inner bins with a bremsstrahlung model plus two Gaussians fixed at the energies of the Fe Heα at 6.67 keV and Fe Heβ at 7.90 keV, leaving the redshift, width, and normalizations of the two lines as free parameters. We find that the Gaussian widths of the Heα line in the two bins are 5.3×10^{-2} keV in the 0.′5–1′ bin and 4.5×10^{-2} keV in the 1′–2′ bin. If we force the Heβ to have a width of up to 8×10^{-2}, the excess due to the Ni Heα line blend at 7.75–7.80 keV is still significantly present. This instrumental effect is evident because of the large equivalent width of the Fe line at 6.67 keV and does not alter significantly the measure of metal abundances, as we show further on.

We can make some other important considerations investigating another line ratio, namely, the Heα Fe line complex at 6.7 keV over the Hα Fe line at 6.97 keV. This ratio allows a robust and independent determination of the temperature, because as the temperature increases the contribution from the He Fe line decreases while the contribution from the H Fe line increases. Thus the intensity ratio of the two lines can be used to estimate the temperature. This was done in the past by determining the variation with the temperature of the centroid of the blend of the two lines, because gas proportional counters did not have sufficient spectral resolution to resolve the two lines (Molendi et al. 1999). With *XMM-Newton* we can now resolve the lines, measure separately their intensity, and use their ratio as a thermometer. To do that we obtain a calibration curve of the line flux ratio as a function of temperature, simulating spectra with the MEKAL model and the PN single response matrix with a step size of 0.1 keV, fixing the metal abundance of 0.3 solar units and the normalization to unity in XSPEC units (however, the flux ratio is independent from these two quantities), with an exposure time of 100 ks to ensure negligible statistical errors. We then model the spectra with a bremsstrahlung model plus two Gaussians for the two iron lines, in the energy range 3–10 keV, obtaining the fluxes of the two lines from the best-fit models. We obtain a calibration curve identical to that of Nevalainen et al. (2003). We then measure the line flux ratio from the cluster PN singles data using the energy range 5.0–7.2 keV to minimize the dependence from the continuum and calibration accuracy and to better describe the lines. We fitted each spectrum with a bremsstrahlung model plus two Gaussians (using the ZBREMSS plus two ZGAUSS models in XSPEC) leaving all the parameters free, including the redshift (to take into account any possible gain calibration problem), except the line energies. The fits for all the annular bins were good, with a reduced χ^2 never worse than 1.1, and the results for the temperature derived from line flux ratio are plotted as diamonds in Figure 2.

As we can also see, this independent temperature determination is in good agreement with all the others at least out to 3′, where the cluster is very bright, and in good agreement out to 8′ with the measurement obtained from the model with the power-law background component, confirming the validity of our modeling. In the last two bins the temperature derived from the lines ratio agrees well with the MECS measurement and starts to differ from the determination with power-law background component, pointing to the fact that our modeling is not sufficient to fully take into account the background in these bins where the source is too dim compared with the soft-proton background. We can conclude that our temperature determination is reliable out to 8′.

The concordance between the lines ratio and the continuum temperature determination adds another piece of evidence against resonant scattering. In fact, since the Fe Hα line optical depth is 1.8 times smaller than the Fe Heα one (this is the difference in their oscillator strength), if resonant scattering is present, we would expect the ratio of Heα/Hα lines to be lower than in the optically thin case. In turn, this would lead to an overestimate of the temperature. Since this is not the case, we can conclude that resonant scattering is not present.

In Figure 5 we plot the abundance profiles of Fe and Ni determined by our best-fit model (thermal model plus power law component for the soft proton background, in the 3–13.5 keV band for PN and 3–12 keV for MOS). We find an evident gradient in both elements: for Fe it agrees well with previous determinations, as with the *BeppoSAX* one (without considering the corrections for resonant scattering, as done in Molendi et al. 1998), while we have for the first time a detailed abundance gradient for Ni, with measurements reliable out to 8′ (we show only the PN data, as discussed before). We stop at this radius because at larger radii the temperature determination is no longer reliable and strong emission lines of Ni, Cu, and Zn induced by particle events affect the spectrum in the crucial range 7.5–8.5 keV (Freyberg et al. 2002). It is evident that there are some problems with the iron determination by MOS1, as we also found in A3528.

Knowing that the excess in the 8 keV line complex is due to the Ni line, we can go back to *BeppoSAX*/MECS data and fit them with a VMEKAL model, allowing Ni abundance to be free. We find an abundance profile in agreement with the more detailed *XMM-Newton* one, as shown in Figure 5.

4.1.1. *Results with the APEC Code*

We try to cross-check the results obtained with the MEKAL code with the ones obtained with the APEC code (Smith et al. 2001). E. Churazov pointed out that the APEC code has different energies for the Ni Heα line complex, resulting in a different fitting for the line.[7] For comparison with Figure 4, we show the fit of the 1′–2′ bin with the recently released APEC

[7] See E. Churazov's presentation to the conference "The Riddle of Cooling Flows in Galaxies and Clusters of Galaxies," held in Charlottesville, VA (2003 May 31–June 4) at http://www.astro.virginia.edu/coolflow/abs.php.

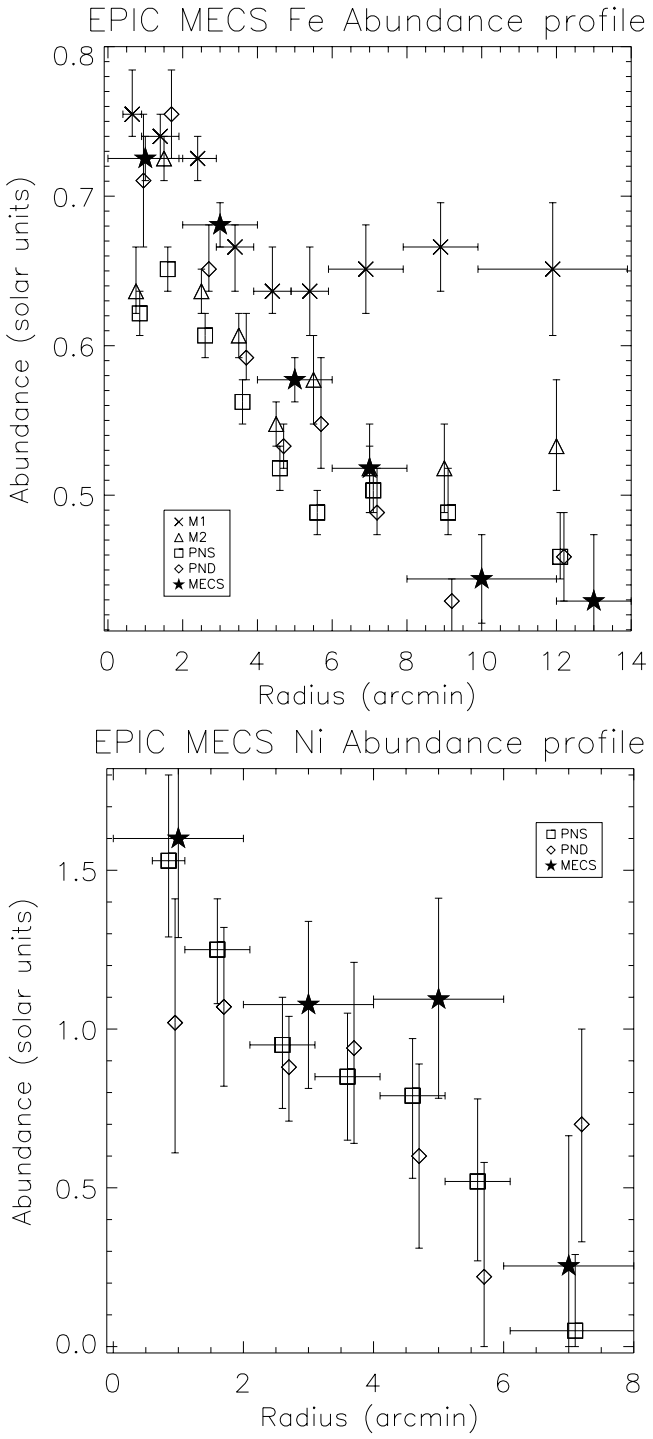

FIG. 5.—Abundance profiles for Fe (*top*) and Ni (*bottom*) obtained with the various EPIC cameras compared with the abundance profiles obtained with the MECS instrument on board *BeppoSAX*. Uncertainties are at the 68% level for one interesting parameter ($\Delta\chi^2 = 1$). As in Fig. 3, crosses refers to MOS1, open triangles to MOS2, open squares to PN singles, open diamonds to PN doubles, and filled stars to MECS.

version 1.3.0 in Figure 6 (but we have to notice that differences in the redshift determination could play a role too: the fit with MEKAL found a redshift of 1.49×10^{-2}, while the fit with APEC found a redshift of 1.54×10^{-2}). The excess is still present, although the statistical improvement of a variable Ni abundance with respect to ratios fixed at solar values is not as evident as in the MEKAL case: the fit with an APEC model gives values of χ^2 of 844 for 802 dof for the $0.'5$–$1'$ bin and 1138 for 1023 dof for the $1'$–$2'$ bin, while a fit with a VAPEC model gives values of χ^2 of 843 for 801 dof for the first bin and 1124 for 1022 dof for the second bin (with a probability of exceeding the F statistic of 3.8×10^{-4} for the second bin). These results are not conclusive, because there are additional issues with APEC, even in this latest release: forbidden and intercombination lines of the He-like Ni triplet are missing, and even after adding these lines, the total Ni emission is still underestimated, thus worsening the differences between APEC and MEKAL and making the excess less evident.[8]

4.2. *1T and 2T Results in the* 0.5–10 keV *Band*

We fit 1T and 2T models to MOS2 and PN single data (we avoid MOS1 data because of the calibration problems explained in the previous section) in the full energy band 0.5–10 keV. One-temperature models cannot adequately fit the entire band spectra, giving temperatures systematically lower than the ones obtained in the hard band and leaving large residuals at high energies. These facts hint of the presence of more than one temperature component; in fact, a 2T model yields a substantially better fit than the 1T model, although it is still not statistically acceptable, as the reduced χ^2 shows in Tables 1 and 2.

The temperature profiles for PN singles data and MOS2 are shown in Figure 7: the 2T fit shows the presence of hot and cold components. The temperature of the hot component, especially in the outer bins, matches the temperature determined with the fit in the hard band, while the temperature of the cold component is less constrained, being about 2 keV in the PN fit and oscillating between 2 and 3 keV in the MOS2 fit. The relative normalization of the two components, shown in Figure 8, shows that the cool component is stronger in the center of the cluster, as we expect for cool core clusters. However, there are some puzzling results, as in the inner two bins of the MOS2 data, where the fitting procedure prefers to give more importance to the cool component, and the presence of cool emission also in the outer bins, where the emission should be negligible (although the cooling radius for Perseus is $\sim 6'$ (Peres et al. 1998).

The Fe abundance profile, shown in Figure 9, is not substantially changed, and in particular the abundance gradient is

[8] See http://cxc.harvard.edu/atomdb/issues_caveats.html.

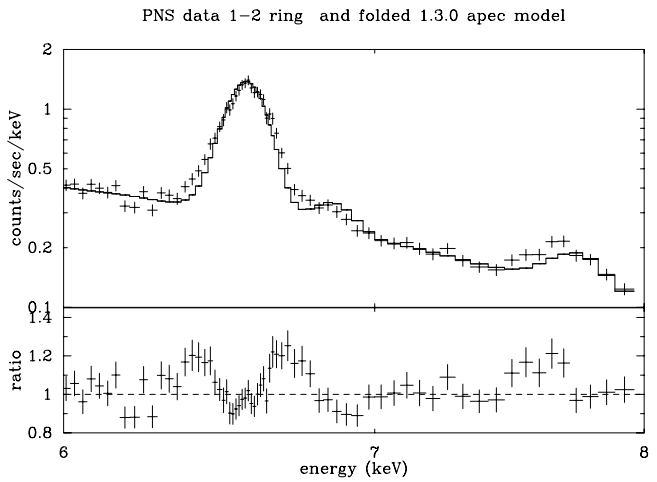

FIG. 6.—PN singles data for the $1'$–$2'$ bin in the 6–8 keV band and the corresponding fit with an APEC model ver. 1.3.0, together with the corresponding ratios of data respect to models.

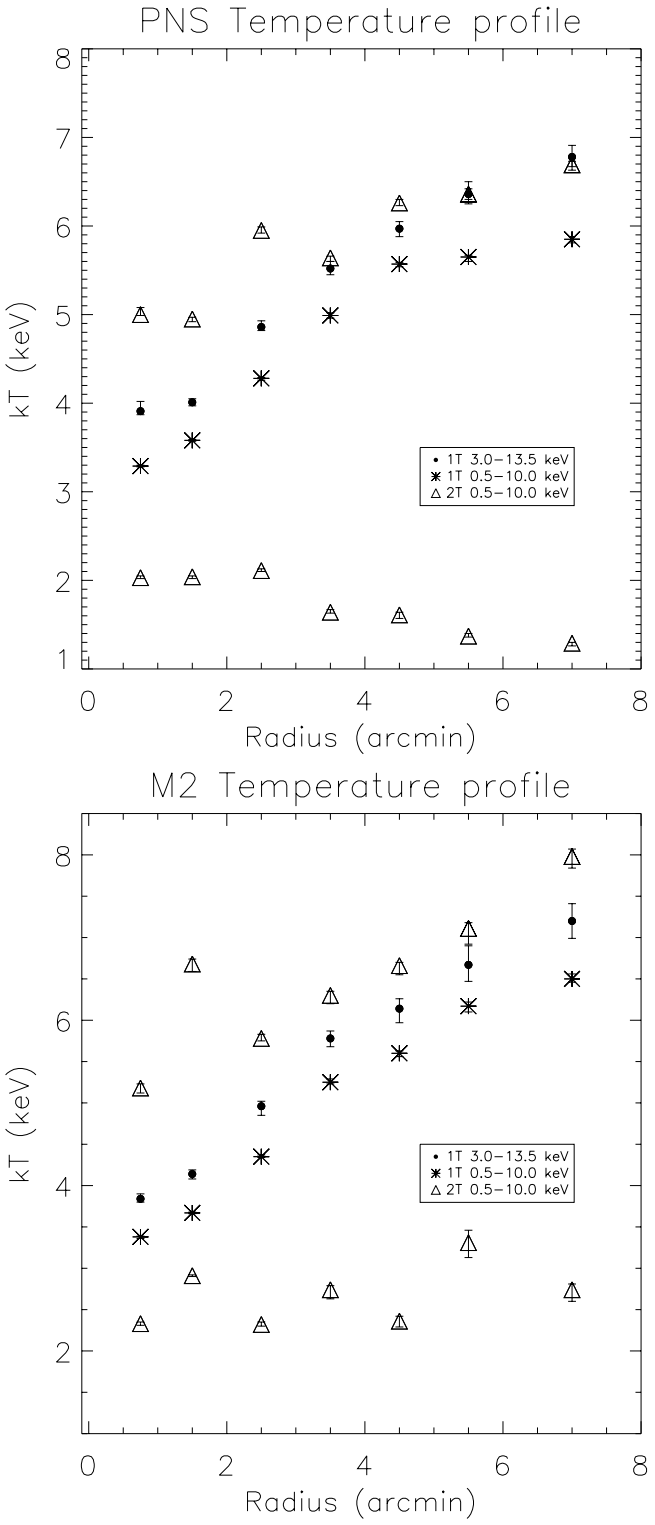

FIG. 7.—Temperature profiles obtained in the entire 0.5–10 keV band using 1T (*crosses*) and 2T models (*open triangles*; the temperatures of both the hot and cold components are shown) and, for comparison, the one obtained with the best-fit model in the hard band (*filled circles*), for PN singles data (*top*) and for MOS2 data (*bottom*). Uncertainties are at the 68% level for one interesting parameter ($\Delta\chi^2 = 1$).

even more evident. Instead, for the Ni abundance profile, shown in Figure 10, the evidence for a gradient is not present. In fact, adding a linear component improves the fit ($\chi^2 = 1.9$ for 5 dof) with respect to a constant ($\chi^2 = 1.9$ for 6 dof) for the PN Ni abundances derived by the 1T model in the hard band, while the Ni profile derived by the 2T model in the entire band is essentially flat (fitting a constant returns a $\chi^2 = 3$ for 6 dof, and a linear component does not improve the fit, $\chi^2 = 2.9$ for 6 dof). We caution the reader that the 2T modelization is rather complex, because some not completely justified assumptions are made, for example, that the abundances of the two components are equal, and there is some degeneracy in the contribution of the two X-ray emission components and the soft-proton power-law background (see for MOS2 and PN the substantial difference in the temperature of the cool component[9]). Therefore, the derived Ni abundance should be taken with some caution. Moreover, it is very difficult to explain, in the presence of a confirmed Fe abundance gradient, a flat Ni abundance profile, and a Ni/Fe ratio that increases going outward.

5. DISCUSSION

Our main result can be summarized as follows: there is no need to invoke resonant scattering in the Fe Heα line in the Perseus Cluster core, and the Fe abundance determination with optically thin emission models is reliable.

Resonant scattering should be important in the core of galaxy clusters, and this is particularly true for the Fe Heα line in the core of the Perseus Cluster (it has an optical depth of 3.3

[9] With the latest release of SAS, ver. 5.4.1, which revises the quantum efficiency for the MOS and the PN, the agreement between the two detectors should be better, in particular in the low-energy band.

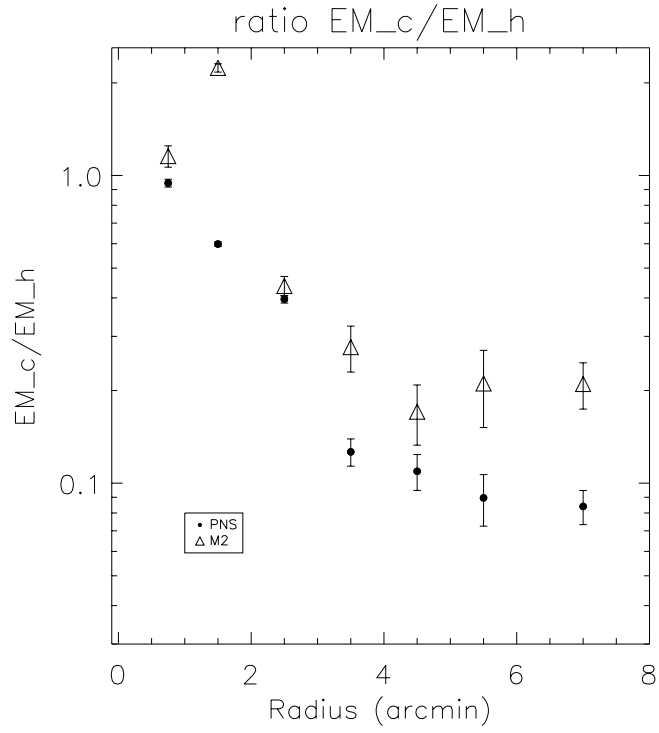

FIG. 8.—Ratio of the normalizations of the two temperature components, obtained by a 2T model fitted in the 0.5–10 keV band, for PN single data (*filled circles*) and MOS2 data (*open triangles*). Uncertainties are at the 68% level for one interesting parameter ($\Delta\chi^2 = 1$).

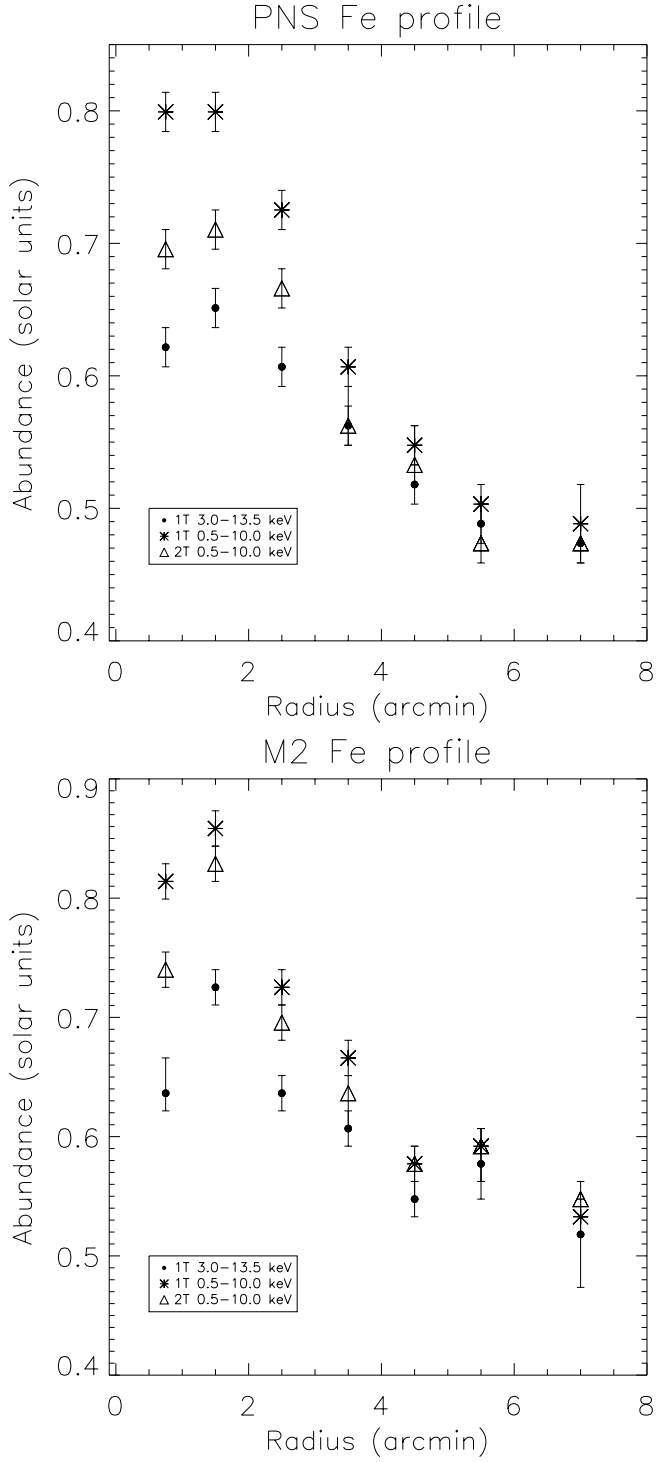

FIG. 9.—Fe abundance profiles obtained in the entire 0.5–10 keV band using 1T (*crosses*) and 2T models (*open triangles*) and, for comparison, the one obtained with the best-fit model in the hard band (*filled circles*), for PN singles data (*top*) and for MOS2 data (*bottom*). Uncertainties are at the 68% level for one interesting parameter ($\Delta\chi^2 = 1$).

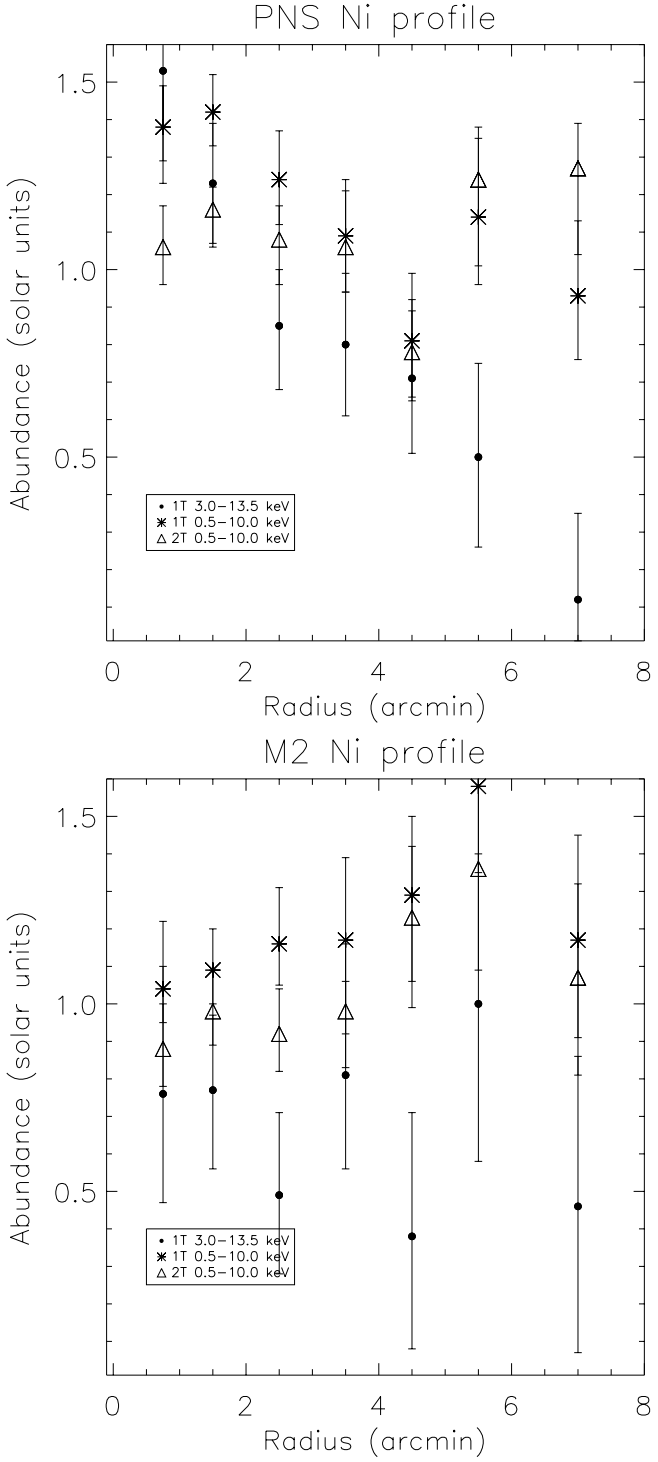

FIG. 10.—Ni abundance profiles obtained in the entire 0.5–10 keV band using 1T (*crosses*) and 2T models (*open triangles*) and, for comparison, the one obtained with the best-fit model in the hard band (*filled circles*), for PN singles data, on the top, and for MOS2 data, on the bottom. Uncertainties are at the 68% level for one interesting parameter ($\Delta\chi^2 = 1$).

according to Sazonov et al. 2002). The optical depth of a resonance line depends on the characteristic velocities of small-scale internal motions, which could seriously diminish the depth τ (Gilfanov et al. 1987; see Mathews, Buote, & Brighenti 2001 for an example of a detailed calculation in presence of turbulent motions). The absence of a clear evidence of resonant scattering strongly points toward the presence of significant gas motions. In fact, following Gilfanov et al. (1987), the optical depth is

$$\tau = \tau^0 (1 + v_{\rm turb}^2 / v_{\rm Fe}^2)^{-1/2}, \quad (1)$$

where τ^0 is the optical depth at the line center in the absence of turbulence (in spectroscopy the word "turbulence" is used

for all hydrodynamic motions of unknown pattern that cause a broadening of the spectral lines; in hydrodynamics "turbulence" has a much more restricted meaning), $v_{\rm turb}$ is the turbulent velocity of the gas, $v_{\rm Fe} = (2kT_e/M_{\rm Fe})^{1/2} \sim c_s/8.8$ is the thermal speed of the iron ions, and c_s denotes the adiabatic sound speed in the intercluster medium. Thus the absence of resonant scattering, $\tau < 1$, and assuming $\tau^0 = 3.3$ (Sazonov et al. 2002) implies gas motions with characteristic velocities greater than 0.36 c_s, i.e., a Mach number $M \gtrsim 0.36$.

Studies of optical line emission in the central regions of elliptical galaxies reveal chaotic gas kinematics, typically about 0.2–0.4 of the sound speed in the hot gas (Caon, Macchetto, & Pastoriza 2000), and since small, optically visible line-emitting regions at $T \sim 10^4$ K are likely to be strongly coupled to the ambient gas, as some models predict (Sparks et al. 1989) and as the clear correlation between Hα+[N II] and X-ray luminosities suggests, the hot gas should share the same turbulent velocities. The first clear example of resonant scattering, acting on the $2p-3d$ line of Fe XVII at 15.0 Å (0.83 keV), has been recently found in the giant elliptical galaxy NGC 4636 (Xu et al. 2002) using the reflection grating spectrometer (RGS) on board *XMM-Newton* and measuring the cross-dispersion profile of the ratio between an optically thin emission blend, the two $2p-3s$ lines of Fe XVII at 17.0–17.1 Å (0.73 keV), and the optically thick line at 15.0 Å. Xu et al. (2002) found that if an average turbulent velocity dispersion more than $\frac{1}{10}$ of the sound speed is added to the assumed Maxwellian, the model becomes incompatible with the ratio of the 17.1/15.0 Å lines. We recall that the detection of the resonant scattering is only in the inner 1′; in fact, the phenomenon does not affect spectra extracted within a full width of 2′ (Xu et al. 2002). Another elliptical, NGC 5044, was observed with the RGS (Tamura et al. 2003), and no evidence of resonant scattering was found in spectra extracted in the full 2′. If in this case a cross-dispersion analysis were also to show resonant scattering, these would rule out possible associations, at least at these inner scales with optically line-emitting gas, because NGC 4636 and NGC 5044 are the most striking examples of chaotic gas kinematics in the sample of Caon et al. (2000).

Another possible source of gas motions is the active glactic nuclus (AGN) activity, which is now thought to be widespread in the core of galaxy clusters and strongly related to hot bubbles, for which one of the best cases is indeed the Perseus Cluster (Fabian et al. 2002). The induced motions could be either turbulent or laminar, as suggested by the recent *Chandra* and optical results in Fabian et al. (2003a, 2003b; see the discussion about the flow causing the horseshoe Hα filament and the derived velocity of 700 km s^{-1}, which for a sound speed of about 1170 km s^{-1}, for a temperature of 5 keV, implies $M \sim 0.6$, and the discussion about the sound waves generated by the continuous blowing of bubbles). AGN activity could also explain the lack of resonant scattering in the other best candidate, M87 (but see also the discussion suggesting caution for this interpretation in the analysis of RGS data for M87 of Sakelliou et al. 2002). What is becoming progressively clearer is that resonant scattering effects must be small and confined on small inner scales.

The Fe abundance gradient confirms the general picture of an increase of SN Ia ejecta in the center of relaxed cD clusters. The determination of the Ni abundance profile is important, because Ni is almost exclusively produced by SN Ia, and also the presence of a gradient in this element could be a crucial confirmation of this general picture (see De Grandi & Molendi 2002b, who report measures of Fe and Ni for a sample of 22 clusters observed with *BeppoSAX*, and in particular their Fig. 6, which shows a segregation between relaxed cD clusters and not relaxed clusters, with the former with greater Fe and Ni abundances with respect to latter). The Ni abundance gradient is evident in the fit in the high-energy band, and looking back at the *BeppoSAX* data, we can attribute the excess in the 8 keV line complex to an increased Ni abundance. However, the complex thermal structure of the gas prevents us from reaching a robust determination of the Ni abundance profile. Detailed temperature and abundances maps are required to address this issue.

S. De Grandi, A. De Luca, F. Pizzolato, E. Churazov, and F. Brighenti are thanked for useful discussion, and the referee is thanked for important suggestions. S. De Grandi is also thanked for kindly providing MECS Ni measurements. This work is based on observations obtained with *XMM-Newton*, an ESA science mission with instruments and contributions directly funded by ESA member states and the USA (NASA).

REFERENCES

Anders, E., & Grevesse, N. 1989, Geochim. Cosmochim. Acta, 53, 197
Arnaud, K.A. 1996, in ASP Conf. Ser. 101, Astronomical Data Analysis Software and Systems V, ed. G. Jacoby & J. Barnes (San Francisco: ASP), 17
Arnaud, M., Neumann, D. M., Aghanim, N., Gastaud, R., Majerowicz, S., & Hughes, J. P. 2001, A&A, 365, L80
Caon, N., Macchetto, D., & Pastoriza, M. 2000, ApJS, 127, 39
Costa, E., Soffitta, P., Bellazzini, R., Brez, A., Lumb, N., & Spandre, G. 2001, Nature, 411, 662
De Grandi, S., & Molendi, S. 2002a, ApJ, 567, 163
———. 2002b, in ASP Conf. Proc. 253, Chemical Enrichment of Intracluster and Intergalactic Medium, ed. R. Fusco-Femiano & F. Matteucci (San Francisco: ASP), 3
Dupke, R. A., & Arnaud, K.A. 2001, ApJ, 548, 141
Fabian, A. C., Celotti, A., Blundell, K. M., Kassim, N. E., & Perley, R. A. 2002, MNRAS, 331, 369
Fabian, A. C., Sanders, J. S., Allen, S. W., Crawford, C. S., Iwasawa, K., Johnstone, R. M., Schmidt, R. W., & Taylor, G.B. 2003a, MNRAS, 344, L43
Fabian, A. C., Sanders, J. S., Crawford, C. S., Conselice, C. J., Gallagher, J. S., III, & Wyse, R. F. G. 2003b, MNRAS, 344, L48
Freyberg, M. J., Briel, U. G., Dennerl, K., Haberl, F., Hartner, G., Kendziorra, E., & Kirsch, M. 2002, in New Visions of the X-Ray Universe in the *XMM-Newton* and *Chandra* Era (ESA SP-488; Noordwijk: ESA)
Fukazawa, Y., Makishima, K., Tamura, T., Nakazawa, K., Ezawa, H., Ikebe, Y., Kikuchi, K., & Ohashi, T. 2000, MNRAS, 313, 21
Gastaldello, F., Ettori, S., Molendi, S., Bardelli, S., Venturi, T., & Zucca, E. 2003, A&A, 411, 21
Gilfanov, M. R., Sunyaev, R. A., & Churazov, E. M. 1987, Soviet Astron. Lett., 13, 3
Grevesse, N., & Sauval, A. J. 1998, Space Sci. Rev., 85, 161
Kaastra, J.S. 1992, An X-Ray Spectral Code for Optically Thin Plasmas (SRON-Leiden Int. Rep., updated ver. 2.0)
Kaiser, C. R. 2003, MNRAS, 343, 1319
Jansen, F., et al. 2001, A&A, 365, L1
Liedahl, D. A., Osterheld A. L., & Goldstein, W. H. 1995, ApJ, 438, L115
Marty, P. B., Kneib, J. P., Sadat, R., Ebeling, H., & Smail, I. 2002, Proc. SPIE 4851, 202
Mathews, W. G., Buote, D.A., & Brighenti, F. 2001, ApJ, 550, L31
Mewe, R., Gronenschild, E. H. B. M., & van den Oord, G. H. J. 1985, A&AS, 62, 197
Molendi, S. 2002, ApJ, 580, 815
Molendi, S., De Grandi, S., Fusco-Femiano, R., Colafrancesco, S., Fiore, F., Nesci, R., & Tamburelli, F. 1999, ApJ, 525, L73
Molendi, S., Matt, G., Antonelli, L. A., Fiore, F., Fusco-Femiano, R., Kaastra, J., Maccarone, C., & Perola, C. 1998, ApJ, 499, 608

Nevalainen, J., Lieu, R., Bonamente, M., & Lumb, D. 2003, ApJ, 584, 716
Peres, C. B., Fabian, A. C., Edge, A. C., Allen, S. W., Johnstone, R. M., & White, D. A. 1998, MNRAS, 298, 416
Pratt, G. W., & Arnaud, M. 2002, A&A, 394, 375
Sakelliou, I., et al. 2002, A&A, 391, 903
Sazonov, S. Yu., Churazov, E. M., & Sunyaev, R.A. 2002, MNRAS, 333, 191
Schmidt, R. W., Fabian, A. C., & Sanders, J. S. 2002, MNRAS, 337, 71
Smith, R. K., Brickhouse, N. S., Liedahl, D. A., & Raymond, J. C. 2001, ApJ, 556, L91
Sparks, W. B., Macchetto, D., & Golombeck, D. 1989, ApJ, 345, 153
Tamura, T., Kaastra, J. S., Makishima, K., & Takahashi, I. 2003, A&A, 399, 497
Xu, H., Kahn, S. M., Peterson, J. R., Behar, E., Paerels, F. B. S., Mushotzky, R. F., Jernigan, J. G., Brinkman, A. C., & Makishima, K. 2002, ApJ, 579, 600